NAVAL POSTGRADUATE SCHOOL

MONTEREY, CALIFORNIA

THESIS

ACTIVE SONAR WAVEFORM DESIGN MATCHED TO A SPHERICAL TARGET AND AN UNDERSEA CHANNEL

by

Justin C. McCorkle

September 2018

Thesis Advisor: Ric Romero
Second Reader: Lawrence J. Ziomek

THIS PAGE INTENTIONALLY LEFT BLANK

REPORT DOCUMENTATION PAGE			*Form Approved OMB No. 0704-0188*

1. AGENCY USE ONLY *(Leave blank)*	**2. REPORT DATE** September 2018	**3. REPORT TYPE AND DATES COVERED** Master's thesis

4. TITLE AND SUBTITLE ACTIVE SONAR WAVEFORM DESIGN MATCHED TO A SPHERICAL TARGET AND AN UNDERSEA CHANNEL	**5. FUNDING NUMBERS**
6. AUTHOR(S) Justin C. McCorkle	
7. PERFORMING ORGANIZATION NAME(S) AND ADDRESS(ES) Naval Postgraduate School Monterey, CA 93943-5000	**8. PERFORMING ORGANIZATION REPORT NUMBER**
9. SPONSORING / MONITORING AGENCY NAME(S) AND ADDRESS(ES) N/A	**10. SPONSORING / MONITORING AGENCY REPORT NUMBER**

11. SUPPLEMENTARY NOTES The views expressed in this thesis are those of the author and do not reflect the official policy or position of the Department of Defense or the U.S. Government.

12a. DISTRIBUTION / AVAILABILITY STATEMENT Approved for public release. Distribution is unlimited.	**12b. DISTRIBUTION CODE** A

13. ABSTRACT (maximum 200 words)

Traditionally, active sonar systems employ an enveloped-continuous wave (CW) or linear-frequency modulated (LFM) acoustic pulse that is transmitted into a lossy channel to interact with the target and environment where the received energy is used to determine if target detection occurs. Many frequency components of a wideband pulse are strongly attenuated due to the effects of the channel and target. In this work, a full-wave solution is used to model a complex channel frequency response. A realistic resonant sphere is used to develop the target response. To exploit the channel-target frequency response, two waveform design techniques are used: signal-to-noise ratio (SNR)-based and information-based methods. Both techniques concentrate the transmit energy in the frequency bands where the target echo is large. The advantage of the eigenwaveform (SNR-based) and the mutual-information (information-based) waveform over the wideband acoustic waveform is the increase in detection probability.

14. SUBJECT TERMS active sonar, eigenwaveform, mutual information, waveform design, waterfilling, spherical target, undersea channel	**15. NUMBER OF PAGES** 59
	16. PRICE CODE

17. SECURITY CLASSIFICATION OF REPORT Unclassified	**18. SECURITY CLASSIFICATION OF THIS PAGE** Unclassified	**19. SECURITY CLASSIFICATION OF ABSTRACT** Unclassified	**20. LIMITATION OF ABSTRACT** UU

NSN 7540-01-280-5500 Standard Form 298 (Rev. 2-89) Prescribed by ANSI Std. 239-18

THIS PAGE INTENTIONALLY LEFT BLANK

Approved for public release. Distribution is unlimited.

ACTIVE SONAR WAVEFORM DESIGN MATCHED TO A SPHERICAL TARGET AND AN UNDERSEA CHANNEL

Justin C. McCorkle
Lieutenant, United States Navy
BS, George Fox University, 2011

Submitted in partial fulfillment of the
requirements for the degree of

MASTER OF SCIENCE IN ELECTRICAL ENGINEERING

from the

NAVAL POSTGRADUATE SCHOOL
September 2018

Approved by: Ric Romero
Advisor

Lawrence J. Ziomek
Second Reader

R. Clark Robertson
Chair, Department of Electrical and Computer Engineering

THIS PAGE INTENTIONALLY LEFT BLANK

ABSTRACT

Traditionally, active sonar systems employ an enveloped-continuous wave (CW) or linear-frequency modulated (LFM) acoustic pulse that is transmitted into a lossy channel to interact with the target and environment where the received energy is used to determine if target detection occurs. Many frequency components of a wideband pulse are strongly attenuated due to the effects of the channel and target. In this work, a full-wave solution is used to model a complex channel frequency response. A realistic resonant sphere is used to develop the target response. To exploit the channel-target frequency response, two waveform design techniques are used: signal-to-noise ratio (SNR)-based and information-based methods. Both techniques concentrate the transmit energy in the frequency bands where the target echo is large. The advantage of the eigenwaveform (SNR-based) and the mutual-information (information-based) waveform over the wideband acoustic waveform is the increase in detection probability.

THIS PAGE INTENTIONALLY LEFT BLANK

Table of Contents

List of Figures

List of Tables

THIS PAGE INTENTIONALLY LEFT BLANK

List of Acronyms and Abbreviations

ASUW anti-surface warfare

ASW anti-submarine warfare

AWGN additive white Gaussian noise

CW continuous wave

DoD Department of Defense

DSP digital signal processing

ESD energy spectral density

ESV energy spectral variance

FT fractional thickness

HE high explosive

INR interference-to-noise ratio

LFM linear-frequency modulated

LTISV linear, time-invariant, space-variant

MI mutual-information

NPS Naval Postgraduate School

PSD power spectral density

SINR signal-to-interference-plus-noise ratio

SNR signal-to-noise ratio

SS stainless steel

SSP sound-speed profile

TS target strength

UUVs unmanned undersea vehicles

Acknowledgments

I would first like to thank my thesis advisor, Dr. Romero of the Electrical and Computer Engineering Department at the Naval Postgraduate School. The door to Prof. Romero's office was always open whenever I had a question about my research, and his email responses were always prompt and helpful. He was consistently patient with me and provided timely course corrections that allowed this experience to be a real pleasure.

I would also like to acknowledge Dr. Ziomek of the Electrical and Computer Engineering Department at the Naval Postgraduate School as the second reader of this thesis, and I am gratefully indebted to him for his guidance and his very valuable comments on this thesis.

Finally, I must express my very profound gratitude to my wife for providing me with unfailing support and continuous encouragement throughout my years of study and through the process of researching and writing this thesis. I am also grateful for the patience that my five beautiful children displayed while I was busy with this endeavor. This accomplishment would not have been possible without them. Thank you.

THIS PAGE INTENTIONALLY LEFT BLANK

CHAPTER 1:
Introduction

The focus of the work presented in this thesis is to apply matched illumination techniques to active sonar waveform design. Matched illumination is a relatively new technique that has been utilized in radar design, but active sonar systems can also benefit from the optimization of transmit waveforms to increase detection probability P_D or received information.

The operational theory of active sonar is very similar to radar. Active sonar systems generate pulses of acoustic energy that propagate into the undersea channel. The acoustic energy scatters off an undersea target, propagates back to the acoustic receiver, and the return energy is collected in the receiver. The acoustic energy of the backscattered return is converted to an electrical signal and compared to some threshold to determine if a target is present.

Active sonar systems are used in many types of undersea missions by many platforms including unmanned undersea vehicles (UUVs), submarines, helicopters, surface ships, and maritime patrol aircraft. Many missions can benefit from active sonar including naval mine-hunting missions, anti-submarine warfare (ASW) and anti-surface warfare (ASUW) operations, seafloor and bottom contour mapping, search and rescue, collision and obstacle avoidance, and navigation. While useful for all of these missions, active sonar is not without its disadvantages. Counter detection is of concern to some platforms, especially submarines. By transmitting acoustic energy into the water, enemy forces can detect the transmitting platform's presence and even determine the source location.

The undersea environment presents a complicated wave propagation problem that often cannot be solved easily. Rigorous, closed-form solutions are sometimes not available. Simplifying assumptions that are often used in electromagnetic wave propagation problems, such as the free-space assumption of some wireless environments, simply do not apply to the ocean waveguide for acoustic signals. The underwater environment is unique because of the varying speed of sound in the medium, the chemical composition of the water, the surface roughness, the bottom composition, and many other factors that all contribute to losses. All of these properties of an undersea channel result in attenuation that is dependent on the following factors: frequency, range, location of the receiver and transmitter in the

water column, and waveguide properties [1]. All of these waveguide factors contribute to an undersea channel's frequency response. In this thesis, the undersea channel's frequency response is modeled using a full-wave solution as presented in [2] and generalized further in [3]. The channel frequency response is just one aspect that determines the frequency spectrum of the received active sonar pulse.

The undersea target also plays an important role in shaping the return signal's frequency spectrum. The target's scattered acoustic field is not only a function of the frequency spectrum of the transmitted pulse but also a function of the size and shape of the target. Additionally, the component materials and orientation of the target in the water column contribute to the frequency spectrum of the scattered acoustic field. For the purposes of this investigation, a resonant sphere is considered, and the scattered field is found utilizing the method described in [4] and [5].

The frequency responses of the undersea channel and target act to severely alter the frequency spectrum of the transmitted pulse. The attenuation in the transmit signal's frequency spectrum results in unrecoverable spectral energy.

1.1 Current Active Sonar Waveform Design

Traditionally, active sonar systems employ an enveloped continuous wave (CW) or linear-frequency modulated (LFM) acoustic pulse that is transmitted into a lossy channel to interact with the target and environment, and the received energy is used to determine if a detection occurs. Transmission in this type of channel results in a considerable amount of attenuated energy in many frequency bands that degrades the overall received signal energy, as described above, which in turn degrades P_D. It is desirable to only transmit those frequency components that are least attenuated to maximize the energy incident on the receiver hydrophones. By not wasting transmit energy in the severely attenuated frequency bands, higher P_Ds can be obtained for a given transmit energy.

The ramifications of using optimized waveforms are not limited to increases in P_D. Currently, a UUV can be fitted with on-board sonar suites that can accomplish an array of missions. Energy storage is a challenge inherent in modern-day UUV operations and will remain so for the foreseeable future. Active sonar hydrophones convert electrical energy into acoustic energy, so if higher acoustic energy is required to achieve a certain level of per-

formance, the electrical demand on the host platform's power storage system is increased. An active sonar system that can operate with similar performance metrics but with lower electrical energy requirements is highly desirable.

Depending on the mission, the expected target and undersea channel combination will have a unique frequency response. This unique frequency response can be exploited to optimize the transmitted waveform to increase P_D.

1.2 Our Approach

The notion of matched illumination has been used in radar waveform design and can also be applied to underwater acoustic waveforms. The two matched illumination design methods that are employed in this thesis are the eigenwaveform and the mutual-information (MI) techniques.

The eigenwaveform technique designs a transmit waveform that maximizes the signal-to-noise ratio (SNR) as described in [6]. This technique generates an optimized waveform by selecting the eigenfunction associated with the largest eigenvalue of the channel-target impulse response. The resulting eigenfunction contains energy in the narrow dominant frequency band or bands of the channel-target frequency response. This SNR-optimized transmit waveform is more effective and results in a higher P_D for an equal amount of energy used in traditional waveforms [6]. Alternatively, the optimized transmit waveforms can achieve similar detection probabilities while using less energy than the traditional waveforms.

The second matched-illumination technique does not attempt to maximize SNR. The information-theoretic technique maximizes the received channel-target MI [6]. This is achieved by "waterfilling" the available transmit energy or power in the dominant frequency bands of the channel-target frequency response [6]. By sending acoustic energy into only the dominant bands of the channel-target frequency response, the return signal's energy is increased. The MI transmit waveform's return energy increase is not as dramatic as the eigenwaveform, but the MI is drastically increased.

To quantify the performance gain of the optimized waveforms in terms of P_D, we compare their P_D against a wideband sonar pulse's performance. It is shown that the P_D of these

waveforms are superior to the wideband pulse's performance.

1.3 Objective

The objective of this thesis is to demonstrate the P_D gains that the eigenwaveform and MI waveform design techniques provide for an active sonar system. To achieve this objective, an undersea target's frequency response is developed using a numerical solution for a resonant sphere given in [4] and [5]. Then, a waveguide's frequency response is numerically determined using the full-wave solution given in [2], [3]. The total system frequency response is modeled to include both transmit and return paths of the channel. Thermal noise and stochastic ambient noise with a power spectral density (PSD) modeled after the Wenz curve are generated and incorporated into the simulated received signal. The optimized waveforms are designed with varying transmit energy constraint E_x. These transmit waveforms are simulated to illuminate the total system with the thermal and ambient noise added. A detection is determined based on a comparison of a calculated test statistic (based on the sonar echo) to a threshold. The matched illumination techniques described previously are implemented via MATLAB simulations to determine the improvement in P_D using Monte Carlo simulations. The simulated results are compared to the theoretical P_D expression to validate the results of the Monte Carlo simulations. Finally, the P_D improvement is demonstrated for the optimized waveforms.

1.4 Thesis Organization

This thesis is organized into six chapters. The signal modeling of the resonant spherical mine-like target, the undersea waveguide, and the random thermal and ambient noise is presented in Chapter 2. The algorithms used to generate the eigenwaveform and MI transmit waveforms are described in Chapter 3. The detection probability calculations are shown in Chapter 4. The results of the Monte Carlo simulations and the corresponding validation by the theoretical equations are provided in Chapter 5. Finally, the conclusion and recommendations are provided in Chapter 6.

CHAPTER 2:
Signal Modeling

Undersea mine detection is just one of the many missions where active sonar is utilized in the undersea environment. Many platforms including submarines, UUVs, and surface ships utilize active sonar. Mines have been designed with varying sizes, shapes, and material compositions, and can be employed almost anywhere in the water column. The scattered fields of an undersea resonant sphere are found using elastic theory as described in [4] and [5].

2.1 System Model

The acoustic energy that is incident on the receiver is a function of the undersea-channel frequency response of the outgoing channel $H_1(f)$, the backscatter target frequency response $C(f)$, and the return undersea channel frequency response $H_2(f)$. We use a linear, time-invariant, space-variant (LTISV) model as shown in Fig. 2.1. In this thesis, we consider a monostatic active sonar problem. Even considering the monostatic problem, the frequency responses of the outgoing and return channels can easily be different.

The LTISV system model shown in Fig. 2.1 simplifies the problem by leaving out any time-varying effects such as movement of the transmitter, the receiver, or the target. The transmit signal $x(t)$ travels through the outgoing channel, interacts with the target, and is scattered back through the return channel. The signal that is incident on the receiver hydrophones $y(t)$ is a superposition of the received backscattered signal and the total noise signal $n(t)$. The noise signal is composed of system thermal noise and ambient noise. Ambient noise is composed of man-made, environmental, and biological sources. The time-domain signals $x(t)$, $y(t)$ are represented in the frequency domain by Fourier transform. The frequency-domain signals are $X(f)$, $Y(f)$. The noise signal $N(f)$ is the Fourier transform of the realization of the superposition of the stochastic random thermal and ambient noise signals. The frequency response of the target is $C(f) = S_s(f, \theta)$ where $S_s(f, \theta)$ is described in Sec. 2.2.1.

The generation of the frequency responses in this thesis is performed in MATLAB. The

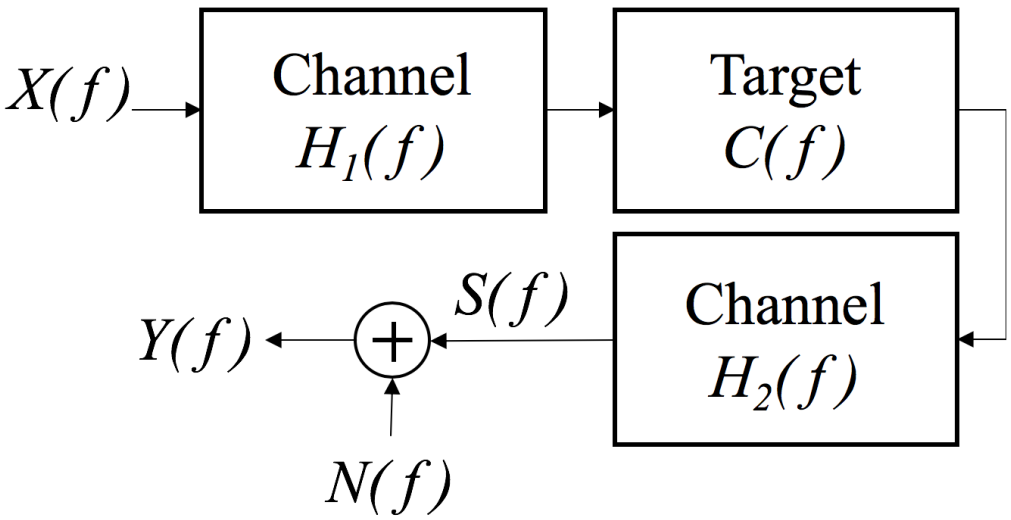

Figure 2.1. Signal Model for an Undersea Channel and Target with Additive Noise

discrete-sampled responses were generated in the frequency range from 0.0 Hz to 10.0 kHz. This frequency range covers the range of low-frequency and medium-frequency active sonar systems. The sampled responses are normalized in the frequency domain to a dimensionless range from 0 to 1. The energy of the responses are retained by scaling the magnitude. All energy spectral density (ESD) plots presented in this thesis are reported in normalized frequency. The Y-axis of the plots are understood to be energy.

2.2 Target Model

Early 20^{th}-century naval mines were often simple spherical shells. As mine technology advanced throughout the century, naval mines took on many shapes. For this thesis, a resonant spherical shell is modeled. Acoustic textbooks typically address the case of a rigid sphere that has an idealized frequency response [1] that is not realistic. By modeling a resonant spherical shell, we find that interesting and more realistic frequency responses arise from the resonances generated by the elastic materials.

2.2.1 Resonant Sphere Model

The interaction of the non-rigid, elastic materials gives rise to resonances that are unique to each configuration of the sphere. It is expected that signals with varying wavelengths incident on a surface with some size, shape, and resonant characteristics will be scattered differently.

To model a naval mine of early 20^{th}-century design, a spherical shell is modeled with the material properties of a common metal like stainless steel (SS) or aluminum. The spherical shell is modeled to contain a substance possessing the material properties of a commonly used high explosive (HE) to represent the explosive charge inside the shell. A diagram of the sphere's cross-section is shown in Fig. 2.2.

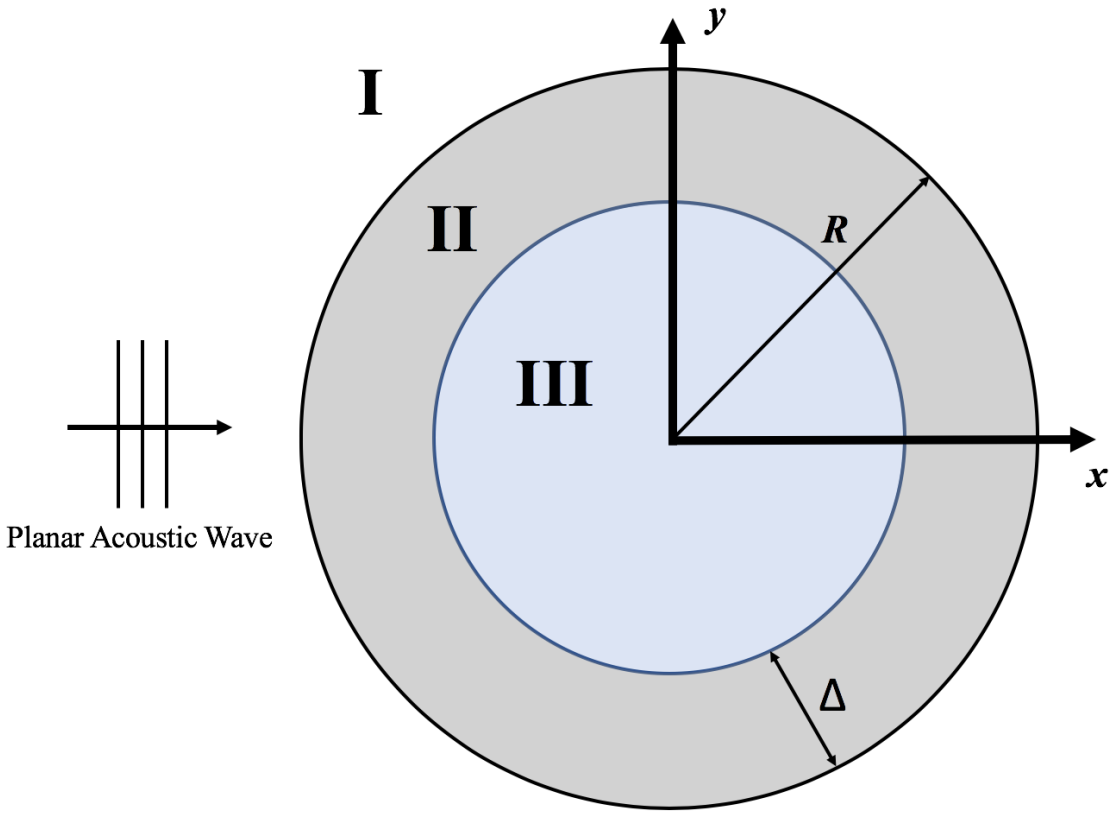

Figure 2.2. Resonant Sphere Model Diagram. Adapted from [4].

For the purposes of this thesis, region I is seawater, region II is metal, and region III is the HE material modeled after the commonly used Composition-B [7]. The fractional

thickness (FT) is calculated as

$$\mathrm{FT} = \frac{\Delta}{R}. \tag{2.1}$$

The magnitude of the FT has a large effect on the frequency spectrum of the sphere's scattered acoustic wave. The method described in [4] and [5] numerically solves for the velocity potential in any region; but for our investigation, we are interested in the scattered acoustic wave in region I. For a spherical target, the general solution for the scattered field is given in

$$\begin{aligned} p_{scat} &= P_0 \sum_{m=0}^{\infty} i^m (2m+1) b_m P_m(\cos\theta) h_m^{(1)}(kr) \\ &= P_0 \frac{e^{ikr}}{r}\Big(-\frac{i}{k}\Big) \sum_{m=0}^{\infty} (2m+1) b_m P_m(\cos\theta), \;\; kr \gg 1, \end{aligned} \tag{2.2}$$

$$k = \frac{2\pi f}{c}, \tag{2.3}$$

where m is the modal number, $P_m(\cos\theta)$ is the Legendre polynomial with spherical vertical angle θ, b_m are the coefficients of the scattered wave as calculated in [4], k is the wavenumber for the surrounding seawater, $h_m^{(1)}(kr)$ is the mth-order Hankel function of the first kind, and r is the range from the sphere to the receiver [5].

The component material's elasticity, the sphere's radius, and the thickness of the shell are encapsulated in the b_m coefficients. The solution involves solving for the boundary conditions between the regions in the sphere with six independent equations with six unknowns in the form of a ratio of two 6×6 determinants using Cramer's rule [5]. The solutions to b_m are obtained in [4] and [5]. In [4] the materials for region I and region III were assumed to be identical. Using the modifications for the coefficients b_m provided in [5], we generalized the spherical model to allow for non-identical material properties in regions I and III.

The far-field limit is given in the limiting form of the Hankel function [5]

$$h_m^{(1)}(kr) \approx (1/kr)\exp(i\,[kr - (m+1)\pi/2]), \;\; kr \gg 1. \tag{2.4}$$

The scattering amplitude S_s can be found using (2.2), yielding

$$S_s(f,\theta) = \frac{-i}{k}\sum_{m=0}^{\infty}(2m+1)b_m P_m(\cos\theta) \tag{2.5}$$

where f is frequency in Hz, θ is the spherical vertical angle, and c is the speed of sound in seawater in $\mathrm{m\,s^{-1}}$ [5].

The results in [4] and [5] and (2.5) are used to generate the frequency spectrum of the scattering amplitude function of the resonant sphere. The target strength (TS) of a resonant sphere is found using [5] where $\theta = \pi$ and $\cos\theta = -1$:

$$\mathrm{TS} = 10\log|S_s(f,\theta)|^2,\ \theta = \pi. \tag{2.6}$$

The TS curves for multiple spheres with varying parameters are generated. The TS curves are normalized so that the maximum value is 0 dB. The parameters of the spheres used to create Figs. 2.3 and 2.4 are listed in Table 2.1. For each sphere in Table 2.1, R is the radius shown in Fig. 2.2, and FT is given in (2.1).

Table 2.1. Sphere Parameters

Sphere	R(m)	FT	Shell Material
A	0.43	0.05	SS
B	0.43	0.10	SS
C	0.86	0.05	SS
D	0.43	0.10	Aluminum

Sphere A is the sphere that is used for the P_D simulations and calculations in the later chapters of this thesis. It is seen that varying the parameters of the sphere changes the TS which depends on the scattering amplitude function. These effects are demonstrated in Figs. 2.3 and 2.4. With the use of (2.5), (2.2) can be written as

$$p_{scat} = P_0\frac{e^{ikr}}{r}S_s(f,\theta) \tag{2.7}$$

where P_0 is the amplitude of the incident acoustic pressure in Pascals. The scattered acoustic pressure field is converted to normalized frequency, and a transducer constant K_t is used to

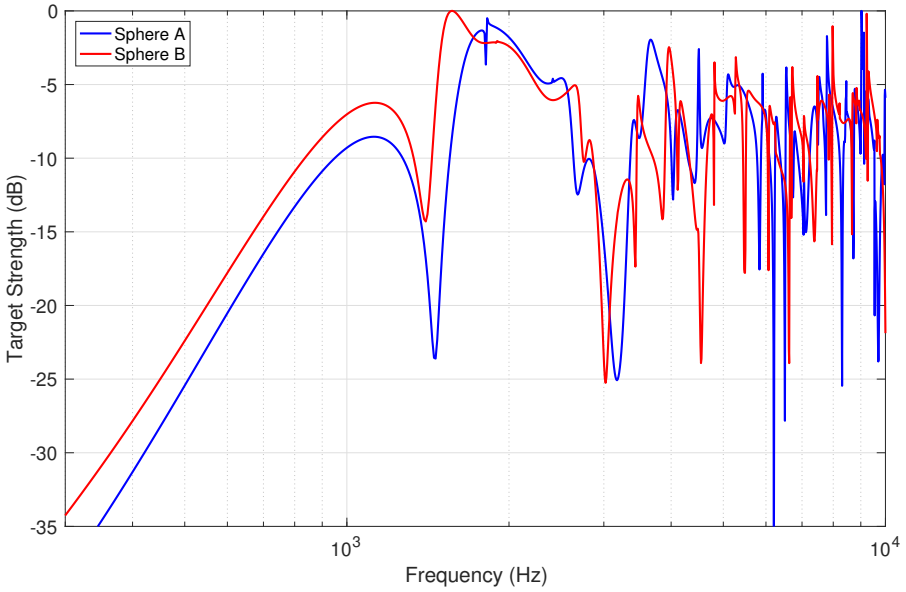

Figure 2.3. Target Strengths for Spheres A and B

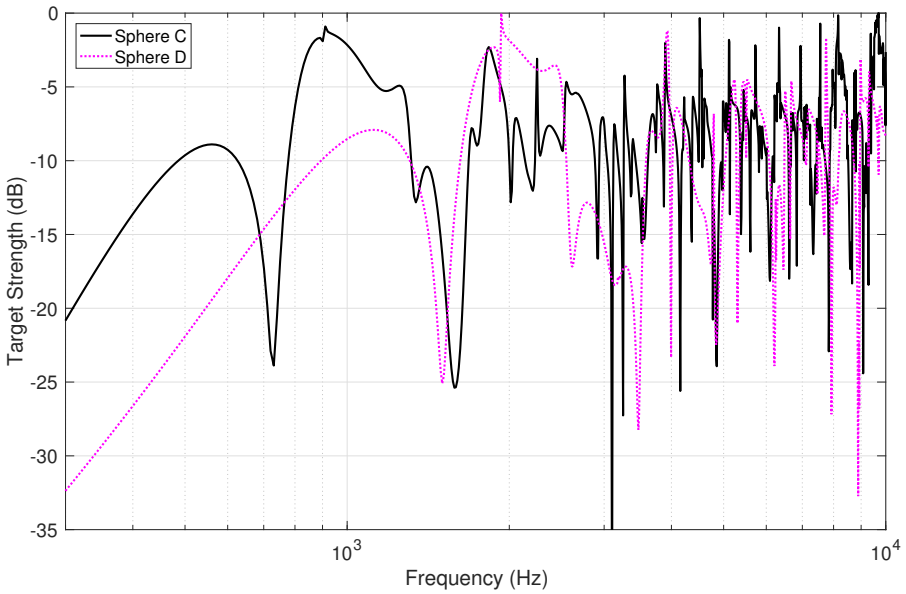

Figure 2.4. Target Strengths for Spheres C and D

convert the acoustic pressure incident on the hydrophones into a voltage. For simplicity, we use $K_t = 1V/Pa$. The corresponding ESD of sphere A is shown in Fig. 2.5. The target's

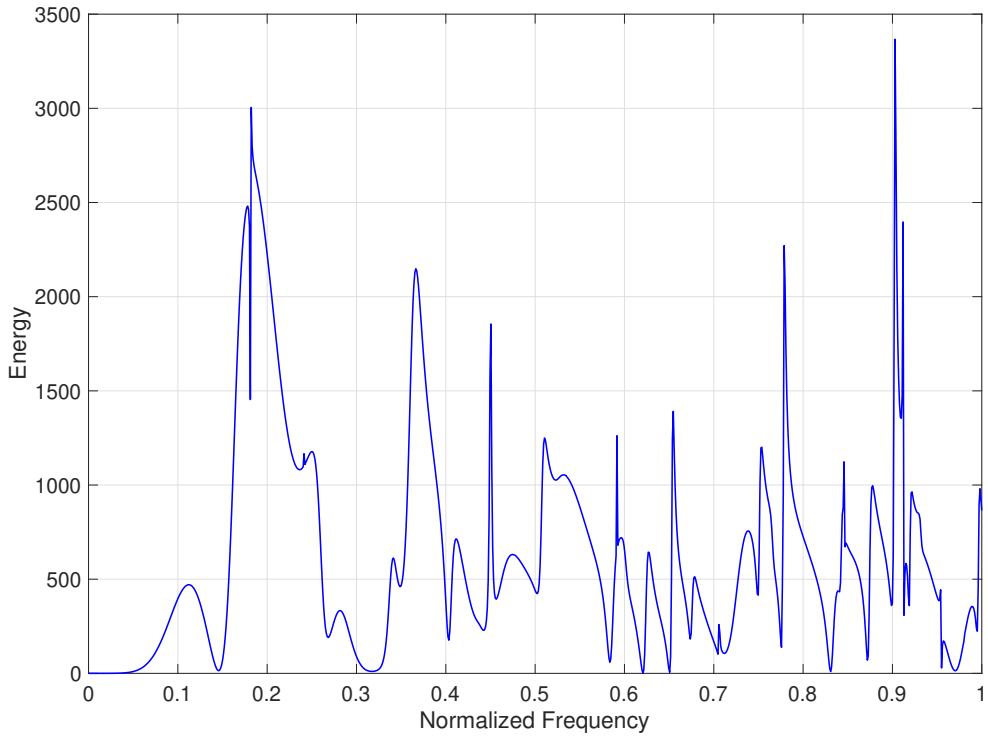

Figure 2.5. Sphere A ESD

frequency response contains frequency bands that are scattered strongly and others that are severely attenuated. The interesting and unique shape of the target's frequency response can be exploited to design a waveform that maximizes the target's scattered acoustic energy into the receiver and, therefore, increases P_D.

2.3 Undersea Channel Model

There are many methods to develop the frequency response of an undersea channel. For the purpose of this thesis, a rigorous solution is desired that is able to account for multi-path propagation. Also, it is desired to utilize unique attenuation coefficients in the model parameters for the air, seawater, and seafloor regions.

In most ocean environments, the sound-speed profile (SSP) throughout the column varies due to competing effects of temperature, pressure, salinity, and the mixing of the layers [1]. The drawback to the full-wave solution presented in [2] is the inability to model a varying

SSP. The full-wave solution assumes a constant speed of sound throughout the water column. For the purposes of demonstrating the design of optimized waveforms for an undersea monostatic active sonar scenario, this assumption is deemed to be acceptable.

2.3.1 Full-Wave Solution

A full-wave solution to the ocean *Pekeris* waveguide model is used in this thesis to estimate the channel's frequency response. The schematic of the *Pekeris* waveguide model is shown in Fig. 2.6 with region I (air), region II (seawater), and region III (ocean bottom).

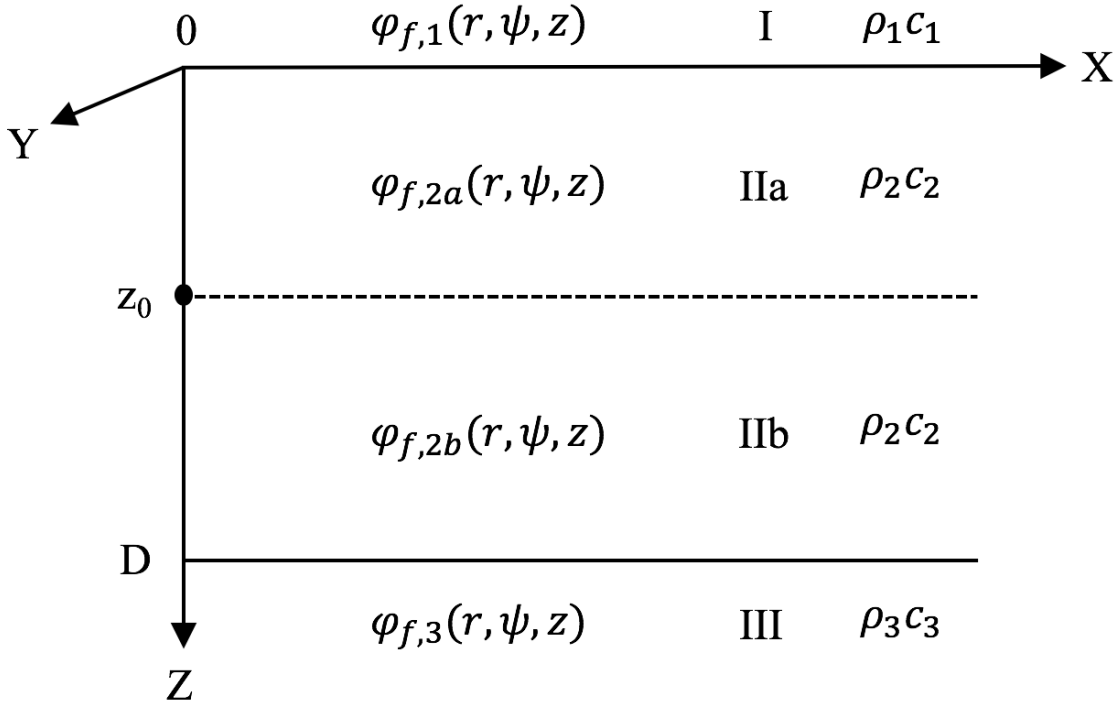

Figure 2.6. Ocean Waveguide Model. Adapted from [2].

The full-wave solution in the ocean waveguide (region II) is equivalent to an infinite sum of "ray integrals" as opposed to normal modes [2]. As a consequence of the infinite sum of the ray-integrals, the full-wave solution accounts for the acoustic reflections that occur at the surface and the seafloor and includes all eigenrays in the multipath propagation [2]. The full-wave solution presented in [2] and used in this thesis allows for any type of ocean bottom composition to be modeled. Additionally, all angles of incidence at the ocean

bottom are accounted for in the full-wave solution [2].

Each region shown in Fig. 2.6 has a characteristic impedance $\rho_i c_i$, $i = 1, 2, 3$, with constant sound speed throughout the water column, where ρ_i is the density of the medium i and c_i is the speed of sound in medium i. Additionally, each medium in the model has an attenuation coefficient α_i that gives rise to frequency and range dependent attenuations [3]. The ocean waveguide has depth D, and the interfaces between the regions are assumed to be parallel [2]. The source is located at depth z_0 and $r = 0$. Region II is further divided into regions IIa and IIb to satisfy the boundary conditions at the source [2]. The velocity potentials in regions IIa and IIb can be determined.

From [2], the reflection coefficients at the ocean surface R_{21} and bottom R_{23} are given by

$$R_{21} = \frac{\rho_1 k_{z_2} - \rho_2 k_{z_1}}{\rho_1 k_{z_2} + \rho_2 k_{z_1}} \tag{2.8}$$

and

$$R_{23} = \frac{\rho_3 k_{z_2} - \rho_2 k_{z_3}}{\rho_3 k_{z_2} + \rho_2 k_{z_3}}, \tag{2.9}$$

respectively, where the propagation-vector components in the Z direction are

$$k_{z_i} = \begin{cases} \sqrt{K_i^2 - k_r^2}, \ k_r^2 \leq \mathrm{Re}\left\{K_i^2\right\}, i = 1, 2, 3, \\ -j\sqrt{k_r^2 - K_i^2}, \ k_r^2 > \mathrm{Re}\left\{K_i^2\right\}, i = 1, 2, 3 \end{cases} \tag{2.10}$$

where

$$K_i = k_i - j\alpha_i \tag{2.11}$$

and

$$k_i = \frac{2\pi f}{c_i}. \tag{2.12}$$

The sign convention for k_{z_i} accounts for the evanescent waves in the negative Z direction in region I and in the positive Z direction in region III [2]. The complex wave number of medium i, K_i, is expressed using the medium's frequency dependent attenuation coefficient α_i as $K_i = k_i - j\alpha_i$, where the real part is simply $k_i = 2\pi f / c_i$ as described in [2] and further developed in [3].

The attenuation coefficient in seawater is determined using the Thorp approximation to the

Francois-Garrison attenuation empirical model for seawater. Generically, the attenuation coefficient for seawater is calculated as

$$\alpha = \left[\frac{0.11}{\left(1 + f^2\right)} + \frac{44}{\left(4100 + f^2\right)} \right] f^2 \tag{2.13}$$

where α is in dB/km and f is frequency in kHz [8]; therefore, $\alpha_2 = \alpha$.

From [2] and [3], the velocity potentials in regions IIa and IIb are given by the following integrals:

$$\begin{aligned} \varphi_{f,2a} = &+ j \frac{S_0}{4\pi} \int_0^\infty \frac{F(k_r, z_0)}{k_{z_2}} \\ &\times \left\{ R_{21} e^{-jk_{z_2}(z+z_0)} + e^{+jk_{z_2}(z-z_0)} \right\} \\ &\times J_0\left(K_r r\right) k_r dk_r, \quad 0 \le z \le z_0 \end{aligned} \tag{2.14}$$

and

$$\begin{aligned} \varphi_{f,2b} = &+ j \frac{S_0}{4\pi} \int_0^\infty \frac{F(k_r, z)}{k_{z_2}} \\ &\times \left\{ R_{21} e^{-jk_{z_2}(z+z_0)} + e^{-jk_{z_2}(z-z_0)} \right\} \\ &\times J_0\left(K_r r\right) k_r dk_r, \quad z_0 \le z \le D \end{aligned} \tag{2.15}$$

where S_0 is the source strength in $\mathrm{m}^3\ \mathrm{s}^{-1}$ and

$$F\left(k_r, z\right) = \frac{1 + R_{23} e^{-j2k_{z_2}(D-z)}}{1 - R_{21} R_{23} e^{-j2k_{z_2} D}}, \tag{2.16}$$

$$K_r = k_r - j\alpha_r, \tag{2.17}$$

and

$$\alpha_r = \alpha_2 k_r / k_2 \tag{2.18}$$

where K_r is the complex wave number in the horizontal radial direction, k_r is the real wave number in the horizontal radial direction, and α_r is the real attenuation coefficient in the horizontal radial direction. The complex reflection coefficients and k_{z_i}, $i = 1, 2, 3$, are defined in (2.8), (2.9), and (2.10), respectively [2], [3]. If the target is located at a

shallower depth than the source, the velocity potential at the target due to the channel is found using (2.14). If the target is deeper than the source, then the velocity potential at the target due to the channel can be found using (2.15). The velocity potentials in (2.14) and (2.15) are converted to acoustic pressure and converted to normalized frequency similar to the target's scattering amplitude function in Sec. 2.2 to effectively yield the channel's frequency responses. An example frequency response for a simulated undersea channel is shown in Fig. 2.7. The frequency response shown in Fig. 2.7 is the result of the full-

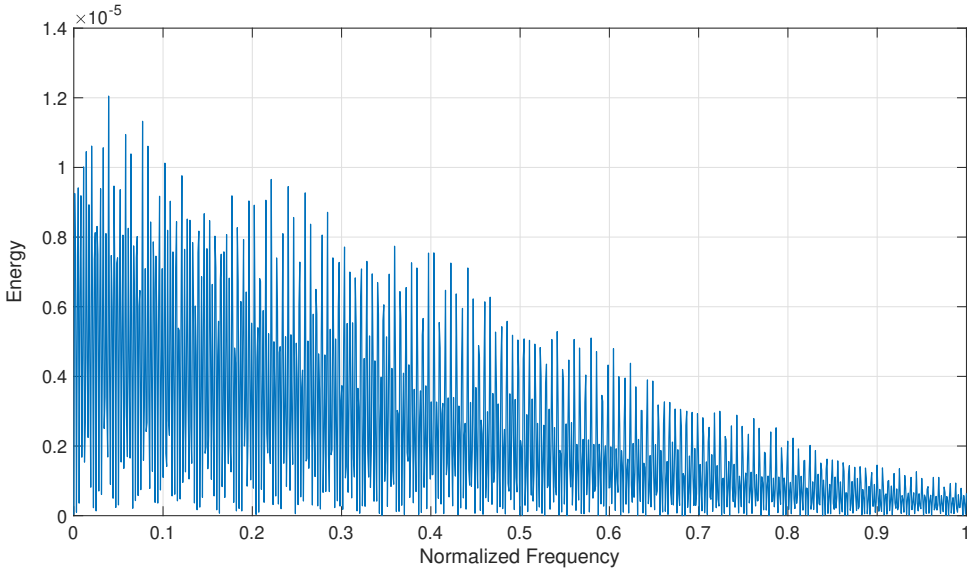

Figure 2.7. Undersea Channel ESD as a Function of Normalized Frequency

wave numerical solution resulting from one leg (direction) of the undersea channel. The waveguide parameters used for the channel's ESD shown in Fig. 2.7 are $D = 500$ m, $z_0 = 400$ m, $z = 300$ m, and $r = 5$ km. This ESD includes the reverberation due to the multi-path propagation and the sea-surface and sea-bottom reflections. It can also be seen in Fig. 2.7 that the ESD for the channel decays as frequency increases due to the frequency-dependent attenuation in seawater.

Referring to the system model defined in Sec. 2.1, we find the total combined frequency response of the channel-target system using frequency-domain multiplication of all three frequency responses considered yielding

$$H_{total}(f) = H_1(f)C(f)H_2(f), \tag{2.19}$$

and the channel-target system's ESD is

$$|H_{total}(f)|^2 = |H_1(f)C(f)H_2(f)|^2, \tag{2.20}$$

where the frequency response of the target scattering amplitude function $C(f) = S_s(f, \theta)$ is found in Sec. 2.2. The channel and target frequency responses are generated in MATLAB. The combined channel-target ESD calculated in (2.20) is shown in Fig. 2.8.

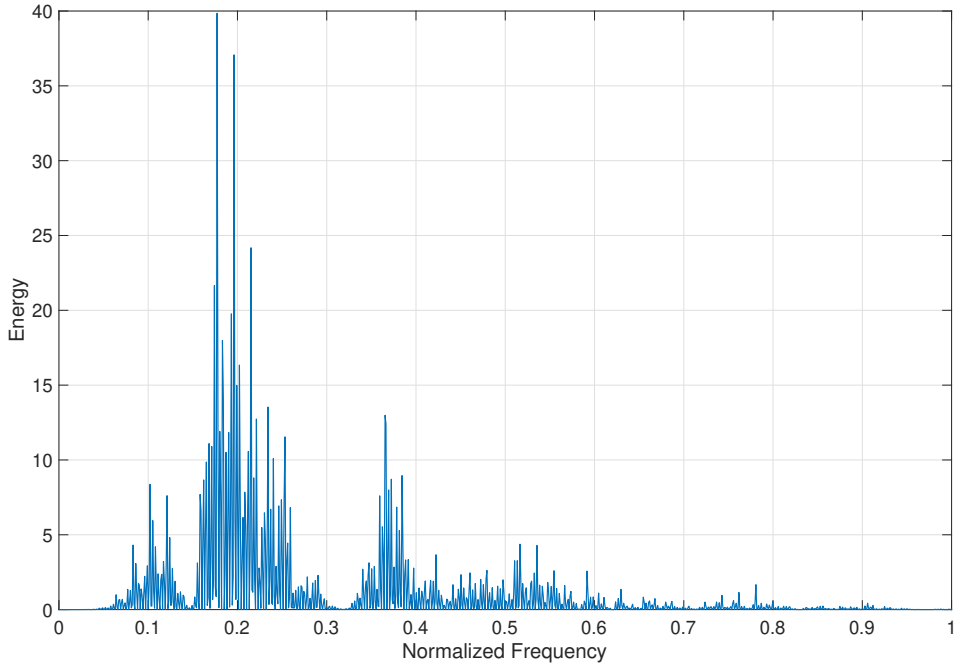

Figure 2.8. Channel-Target ESD as a Function of Normalized Frequency

The competing effects of the channel's high-frequency attenuation and the target's relatively large target strength in the mid-frequency (0.1 to 0.6) range yields an interesting frequency response that can be exploited to increase detection probability.

2.4 Noise Models

All electrical systems have self-noise that is unavoidable and must be considered when receiving and processing low-energy signals. Sonar systems are no different. Additionally,

the ocean is a noisy environment. The ocean ambient noise is composed of man-made sources of energy as well as environmental and biological sources. Man-made sources include shipping vessels and industrial activity like undersea drilling. Environmental noise energy results from precipitation, wind, waves, and seismic activity. Biological activity includes noise energy from whales, dolphins, fish, shrimp, etc. These noise sources result in broad spectrum noise.

To model a realistic undersea environment, these two sources of noise (thermal and ambient), must be accounted for at the receiver with known or estimated statistics that can be used and in fact be exploited when generating the transmit sonar waveforms.

2.4.1 Thermal Noise Model

The amplifier networks connected to acoustic hydrophones contain thermal or *Johnson* noise [1] that must be modeled. All hydrophones and their connected electrical networks have some measurable thermal noise that can be modeled rather simply. For this thesis, the receiver thermal noise is modeled as a complex-valued, additive white Gaussian noise (AWGN). Accordingly, the receiver thermal noise PSD $S_{nn}(f)$ is flat. In the simulations, the discrete-time signals (with unit-time sampling) are utilized to follow the convention in digital signal processing (DSP). As a result, the simulated thermal noise vector has a covariance matrix $\mathbf{R}_{th} = \sigma_{th}^2\mathbf{I}$ where σ_{th}^2 is the sample thermal noise variance, and $\mathbf{I}$ is the identity matrix.

2.4.2 Ambient Noise Model

Unlike the receiver thermal noise which has a flat PSD, the ambient noise PSD has an interesting shape which depends on sea state and other broad spectrum sources of noise in the ocean environment [1]. To generate realistic ambient noise, the Wenz curve [9] is used to model the PSD for a given set of ambient noise parameters. The PSD, shown in Fig. 2.9, is used to create correlated AWGN signals in MATLAB. The random realizations of ambient noise are used in our Monte Carlo simulations to determine detection probabilities. The PSD shown in Fig. 2.9 corresponds to the PSD of the ambient noise $S_{aa}(f)$. The curve in Fig. 2.9 models the ambient noise level of an undersea environment with a sea state 2 and medium shipping traffic. For our simulations, the ambient noise is modeled in discrete time (unit-time sampling) which yields the covariance matrix $\mathbf{R}_{amb}$. Thus, the total noise is

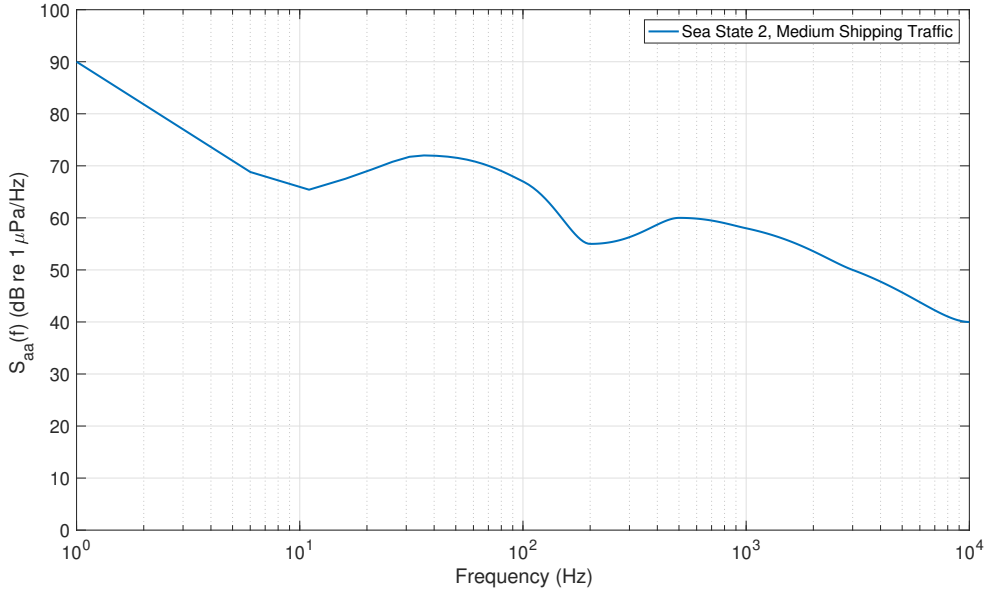

Figure 2.9. Ambient (Wenz) Noise PSD. Modeled after [9].

$\mathbf{w} \sim \mathcal{CN}(\mathbf{0}, \mathbf{C})$ where the total noise covariance matrix is clearly the sum of the two noise covariance matrices as given by $\mathbf{C} = \sigma_{th}^2 \mathbf{I} + \mathbf{R}_{amb}$ [10]. The ambient interference-to-noise ratio (INR) is parameterized by increasing the total power under the Wenz PSD shown in Fig. 2.9. The ambient noise power is scaled relative to the thermal noise power. The thermal noise variance is assumed to be unity. The INR is expressed as

$$\text{INR} = \frac{\int_w S_{aa}(f)df}{\int_w S_{nn}(f)df} \tag{2.21}$$

where w is the effective bandwidth of the transmit signal.

CHAPTER 3:
Optimized Waveforms

The motivation to design optimized waveforms comes from the fact that it is undesirable to transmit acoustic energy that will inevitably be severely attenuated by the channel. The two transmit waveform design techniques used in this thesis differ in what they attempt to optimize. The first technique, the eigenwaveform, maximizes the channel-target SNR. The second technique does not attempt to maximize SNR. The MI waveform optimizes the shared information between the received signal and the channel-target response.

3.1 Wideband Pulse

The optimized waveforms are compared to a wideband pulse. The energy spectrum of the wideband pulse is assumed to be flat across the entire bandwidth. The energy spectrum of an example wideband pulse with $E_x = 2$ is shown in Fig. 3.1. The idealized wideband pulse evenly distributes its entire energy across the bandwidth of interest.

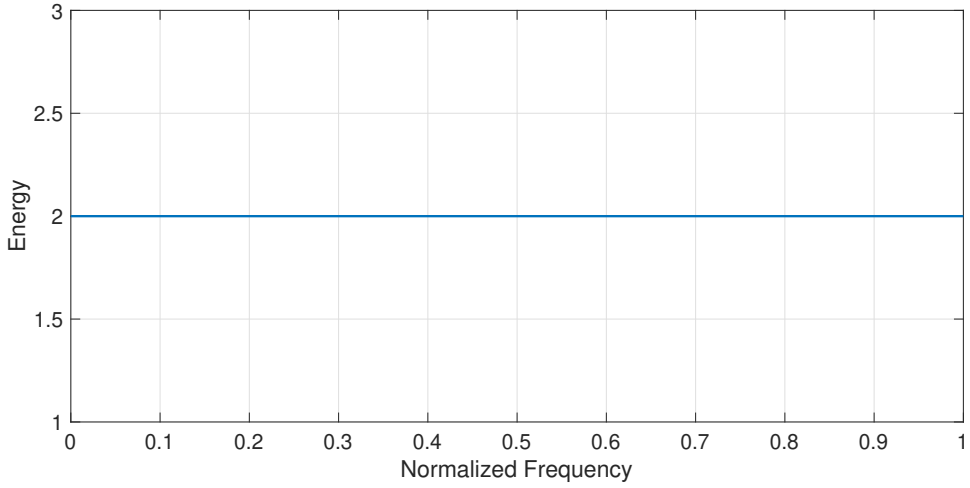

Figure 3.1. Wideband Pulse ESD as a Function of Normalized Frequency

3.2 Eigenwaveform

The eigenwaveform transmit waveform maximizes the SNR of the channel-target system. For the case where only uncorrelated AWGN is present, the SNR can be expressed as

$$\text{SNR} = \int_{-\infty}^{\infty} \frac{|H(f)X(f)|^2}{S_{nn}(f)} df \tag{3.1}$$

where $|H(f)|^2$ is the channel-target ESD, given by (2.20), $|X(f)|^2$ is the transmit signal ESD, and $S_{nn}(f)$ is the thermal noise PSD which is modeled to be flat across the entire bandwidth [6]. For the case when correlated Gaussian (colored) noise is also present, the expression for the signal-to-interference-plus-noise ratio (SINR) can be expressed as

$$\text{SINR} = \int_{-\infty}^{\infty} \frac{|H(f)X(f)|^2}{S_{nn}(f) + S_{aa}(f)} df \tag{3.2}$$

where $S_{aa}(f)$ is the PSD of the ambient noise [11].

The eigenwaveform algorithm generates an optimized transmit waveform for the channel-target frequency response while also accounting for the noise. The optimized complex-valued transmit signal $\tilde{x}(t)$ with a finite duration T to satisfy some transmit energy constraint E_x is defined in [6] by

$$\lambda_{max}\tilde{x}(t) = \int_{-T/2}^{T/2} \tilde{x}(\tau)\, M(t-\tau)\, d\tau \tag{3.3}$$

where λ_{max} is the largest eigenvalue and the kernel $M(t)$ is given by [6], [11]

$$M(t) = \int_{-\infty}^{\infty} \frac{|H(f)|^2}{S_{nn}(f) + S_{aa}(f)} e^{j2\pi ft} df. \tag{3.4}$$

The eigenfunction $\tilde{x}(t)$ corresponds to the largest eigenvalue λ_{max}. As in the case of noise, transmit signals are sampled and normalized sampling time is assumed. In discrete-time, the eigenfunction corresponds to an eigenvector and any transmit vector is referred to as $\mathbf{x}$.

3.3 Mutual-Information Waveform

Mutual information is an informational-theoretic measure used to quantify the amount of shared spectral information between the received signal and the target-channel response.

For a system with thermal noise and ambient noise, the mutual information is given in

$$\mathrm{MI} = \int_w \ln\left[1 + \frac{|X(f)|^2\,\sigma_H^2(f)}{S_{nn}(f) + S_{aa}(f)}\right] df \tag{3.5}$$

where w is the effective bandwidth of the transmit signal and $\sigma_H^2(f)$ pertains to the energy spectral variance (ESV) of the target ensemble [11]. In this thesis, the ESV is replaced by the total target-channel ESD $|H(f)|^2$ from (2.20). The MI waveform is generated by "waterfilling" the available transmit energy into the dominant frequency bands of the channel-target energy spectrum while accounting for the total noise PSD. The energy spectrum of the MI-based optimum transmit signal is

$$|X(f)|^2 = \max\left[0, A - \frac{T\,[S_{nn}(f) + S_{aa}(f)]}{\sigma_H^2(f)}\right] \tag{3.6}$$

where the transmit energy constraint is obeyed via

$$(E_x - \delta/2) \le \int_w \max\left[0, A - \frac{T \cdot S_{nn}(f)}{\sigma_H^2(f)}\right] df \le (E_x + \delta/2) \tag{3.7}$$

where δ is the error tolerance used in forming the waveform, A is the "waterfill" level, and E_x is the transmit energy.

Just as in the SNR based design, we develop our results using discrete-time and discrete-frequency domains. In other words, we can form the discrete-time (with normalized sampling time) transmit vector $\mathbf{x}$ corresponding to (3.6).

THIS PAGE INTENTIONALLY LEFT BLANK

CHAPTER 4:
Detection Probability

In the previous chapters, the frequency responses for the channel and target were found. In this chapter, we refer to the impulse responses of the channel and target. In continuous time and frequency, it is understood that the impulse response is the inverse Fourier transform of the corresponding frequency response. For our simulations, discrete-time and discrete-frequency vectors are utilized; therefore, the impulse responses are generated using the inverse fast Fourier transform (IFFT) of the discrete-frequency vectors. The continuous-time frequency response for the total system response $H_{total}(f)$ becomes $\mathbf{H_{total}}$ in discrete-frequency. The corresponding discrete-time impulse response becomes

$$\mathbf{h_{total}} = \text{IFFT}\left[\mathbf{H_{total}}\right]. \tag{4.1}$$

4.1 Matched Filter Detection

For all P_D calculations, the matched-filter receiver is considered. The transmit vector (eigenvector or MI) $\mathbf{x}$ containing a particular transmit energy E_x is convolved with the total channel-target impulse response $\mathbf{h_{total}}$ (the discrete time-domain vector corresponding to (2.19)). Accordingly, the expression

$$\mathbf{s} = \mathbf{h_{total}} * \mathbf{x} \tag{4.2}$$

is used to determine the transmit-signal, target-channel convolution. The thermal and ambient noise are then added to $\mathbf{s}$ to form the total received signal $\mathbf{y}$ represented as

$$\mathbf{y} = \mathbf{s} + \mathbf{n_{th}} + \mathbf{n_{amb}} \tag{4.3}$$

where $\mathbf{n_{th}}$ is a random realization of thermal noise and $\mathbf{n_{amb}}$ is a random realization of the ambient noise modeled after the Wenz curve presented in Chapter 2, Sec. 2.4.

To determine if a detection occurs, a test statistic is compared to a threshold. From [10],

the test statistic is calculated as

$$T(\mathbf{y}) = \mathrm{Re}\left(\mathbf{s}^H \mathbf{C}^{-1} \mathbf{y}\right). \tag{4.4}$$

The test statistic represents the output of the matched filter and is compared to the threshold γ' which is calculated as

$$\gamma' = \sqrt{\mathbf{s}^H \mathbf{C}^{-1} \mathbf{s}/2}\, Q^{-1}(P_{FA}) \tag{4.5}$$

where Q^{-1} is the inverse Q function and P_{FA} is the false-alarm probability [10]. Formally, the target detection occurs when $T(\mathbf{y}) > \gamma'$.

4.2 Theoretical Expression for Detection Probability

Fortunately, a closed-form P_D expression exists for the case when correlated Gaussian noise is present. An expression is provided in [10] to calculate the P_D for a matched-filter receiver given a noise covariance matrix $\mathbf{C}$. The closed-form solution for detection probability is given by

$$P_D = Q\left(Q^{-1}(P_{FA}) - \sqrt{2\mathbf{s}^H \mathbf{C}^{-1} \mathbf{s}}\right) \tag{4.6}$$

and must be calculated for each E_x increment [12]. The curves generated using this expression are used to validate the Monte Carlo simulations that are described in Sec. 4.3.

4.3 Monte Carlo

In order to determine the P_D gain with the use of the SNR-based eigenwaveforms and MI-based waveforms as promised in (4.6), Monte Carlo simulations are performed to generate P_D curves as a function of the transmit energy to thermal noise variance ratio (E_x/σ_{th}^2). The optimized eigenwaveforms and MI transmit waveforms described in Chapter 3 are generated in MATLAB and the corresponding P_D curves are produced. The wideband pulse described in Sec. 3.1 is used to provide a comparison for P_D peformance. For each transmit-energy value in the Monte Carlo simulation, the eigenwaveform and MI transmit waveform P_D performances are compared to their corresponding theoretical closed-form P_D values calculated using (4.6).

CHAPTER 5:
Results

Monte Carlo simulations are performed utilizing the SNR-based and MI-based transmit waveforms that are simulated to interact with the modeled undersea channel and the resonant spherical target that were previously described. Two false alarm probabilities were considered, $P_{FA} = 10^{-2}$ and $P_{FA} = 10^{-4}$. The thermal noise sample variance is assumed to be unity. The INR is used to parameterize the ambient noise to thermal-noise power ratio. The simulations are performed for INR = 10 dB, 20 dB, and 40 dB.

5.1 Full System Response

The frequency responses of the channel and target are multiplied to generate the total frequency response of the system using (2.19) and shown in Fig. 2.8. The ambient noise PSD, modeled after the Wenz curve, can be visually compared to the channel-target ESD in Fig. 5.1. It is apparent from Fig. 5.1 that there are dominant frequency bands in the channel-target ESD that can be exploited by the eigenwaveform and MI techniques. It can also be observed in Fig. 5.1 that the ambient Wenz noise dominates the low-frequency portion (left-side) of the energy spectrum. Depending on the power of the ambient noise (as dictated by the INR), we expect for the eigenwaveform and the MI waveform algorithms to avoid distributing transmit energy in those noise-dominated and heavily attenuated frequency bands. The result of the higher noise energy in the low-frequency portion of the spectrum effectively "shifts" the transmit waveforms to the higher frequencies.

5.2 Eigenwaveform

Recall that the eigenwaveform distributes all of the the transmit energy in one, or possibly a few, narrow frequency bands that are dominant in the channel-target frequency response.

5.2.1 Eigenwaveform Spectral Content

The transmit waveform designed using the eigenwaveform technique is usually expected to have a single dominant frequency band [6]. The transmit eigenwaveform, shown in Fig. 5.2,

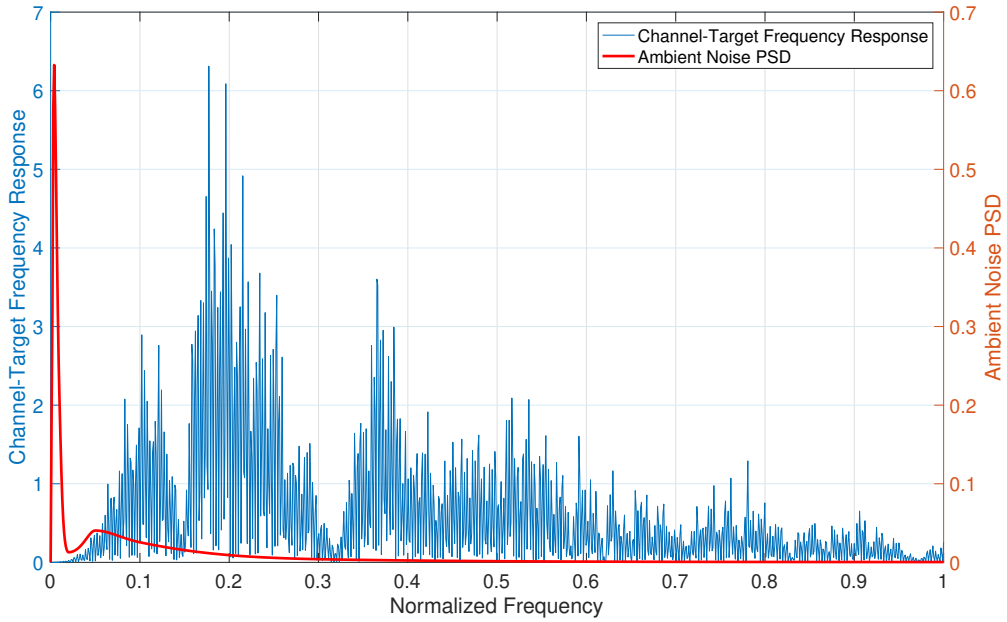

Figure 5.1. Channel-Target Frequency Response with Ambient Noise PSD Superimposed

selects a single narrow dominant band in the spectrum for this specific combination of channel and target responses, INR, E_x, and noise. The eigenwaveform selects the eigenfunction

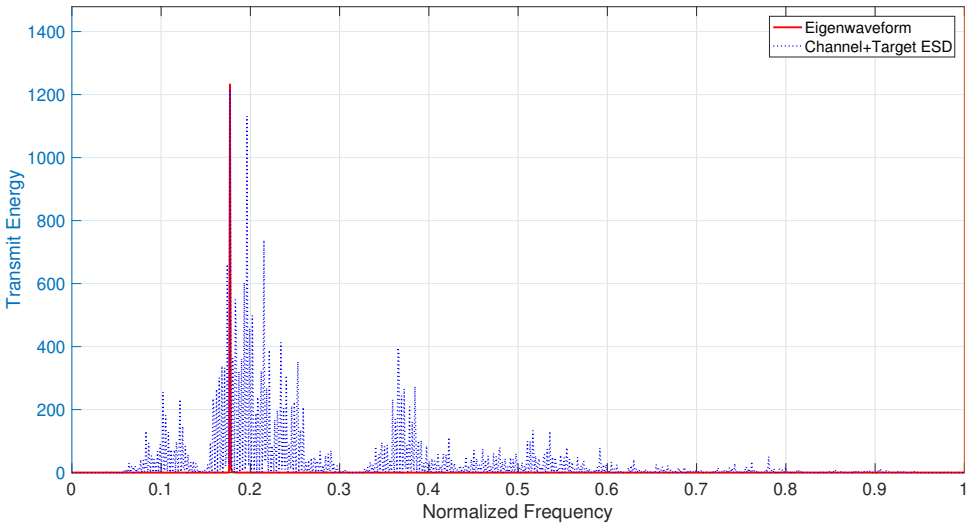

Figure 5.2. Eigenwaveform Transmit Signal ESD

that corresponds to the maximum eigenvalue of the kernel defined in Chapter 3, (3.4). In this case the eigenfunction produces the dominant narrow frequency band shown in Fig. 5.2. This waveform optimizes the SINR that is expressed in (3.2).

5.2.2 INR Comparison

To demonstrate how the eigenwaveform behaves for varying ambient noise levels, transmit waveforms were created using the eigenwaveform technique with identical transmit energies. The channel and target responses are unchanged for each INR iteration, so the only parameter that is changed is the INR. The ambient noise PSD is scaled by a factor of INR relative to the thermal noise PSD. The eigenwaveform is expected to shift in frequency as the INR increases or decreases. It can be seen in Fig. 5.3 that a 10 dB increase in INR causes the eigenwaveform to select a different frequency band. The newly selected frequency band is still affected by the ambient noise but to a much lesser degree than the original frequency band. Because the ambient Wenz noise is dominant in the lower frequencies, an increase in

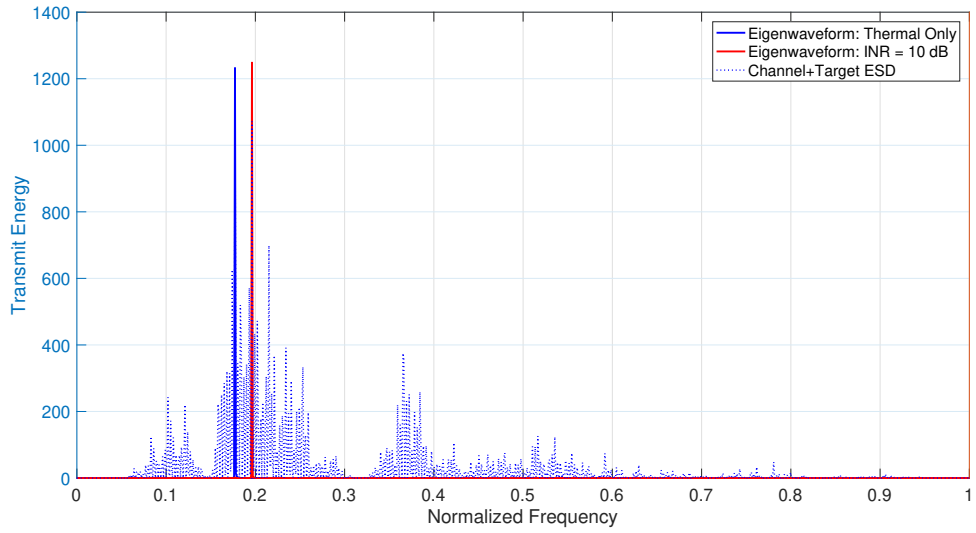

Figure 5.3. Eigenwaveform Transmit Signals for Two Different INRs

the ambient noise level results in the dominant eigenfunction (corresponding to the red line) shown in Fig. 5.3. This suggests that for a given noise environment, the transmit waveform spectrum may change to maximize SNR to optimize detection performance.

5.3 Mutual Information

Unlike the eigenwaveform, the MI waveform is expected to spread the transmit energy or transmit power across several frequency bands [6].

5.3.1 Transmit Power Comparison

In Fig. 5.4, we see how the spectrum of the MI transmit waveform changes as the transmit energy increases. In Fig. 5.4, there are three unique transmit waveforms that are designed for the same channel, target, and noise environment. The only variable that changes between the three waveforms is the amount of transmit energy E_x that the waveform contains. The three transmit energies shown are 1 J, 10 J, and 1 kJ. As the transmit energy increases, the MI algorithm spreads the transmit energy across an increasing number of favorable frequency bands as well as increasing the amplitude of the already selected bands. The algorithm does not distribute transmit energy into those bands that are heavily attenuated in the channel or by the scattering of the target.

5.3.2 Ambient Noise Power Comparison

Similar to the eigenwaveform behavior shown in Fig. 5.3, the MI transmit waveform changes for increasing or decreasing INR. We expect the MI waveform to shift toward the higher frequencies for increasing levels of INR (increasing ambient noise power) due to the noise dominance in the lower frequency range (see Fig. 5.1). The effective shifting of the MI transmit spectrum is observed in Fig. 5.5 where the INR increases from 10 dB to 20 dB and finally to 40 dB. As the ambient noise power increases, the "waterfilling" algorithm begins to distribute more energy across the spectrum into the desirable frequency bands.

5.4 Detection Probability

5.4.1 Thermal Noise Only

In our approach to validate the models used to determine P_D, we first consider a system with thermal noise being the only noise component. In this version of the model, the ambient-noise level is assumed to be zero. It follows that the noise covariance matrix only accounts for the thermal AWGN and is represented as $\mathbf{C} = \sigma_{th}^2 \mathbf{I}$. We see in Figs. 5.6 and 5.7 that the P_D curves generated with the Monte Carlo simulations are validated with the

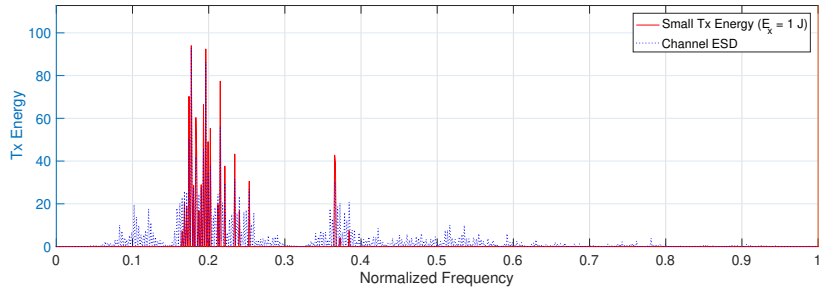

(a) Low transmit power with $E_x = 1$ J.

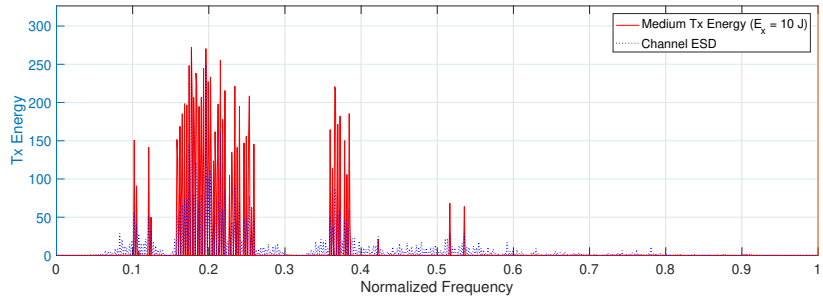

(b) Medium transmit power with $E_x = 10$ J.

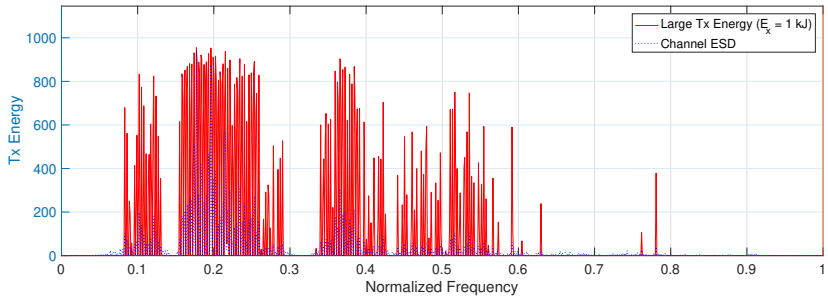

(c) High transmit power with $E_x = 1$ kJ.

Figure 5.4. Mutual-Information Transmit Waveforms with Increasing Amounts of Transmit Energy

theoretical expression for P_D. The theoretical curves are the dotted line curves on the plots.

The P_D gains of the optimized waveforms for each false-alarm probability P_{FA} values are summarized in Table 5.1. The gains listed in Table 5.1 pertain to a $P_D = 0.9$.

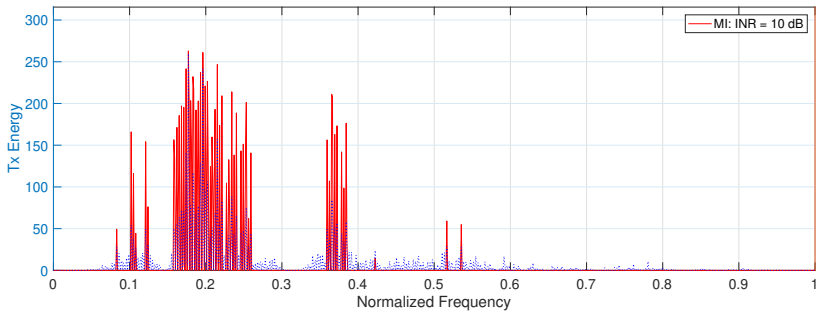

(a) E_x = 100 J and INR = 10 dB.

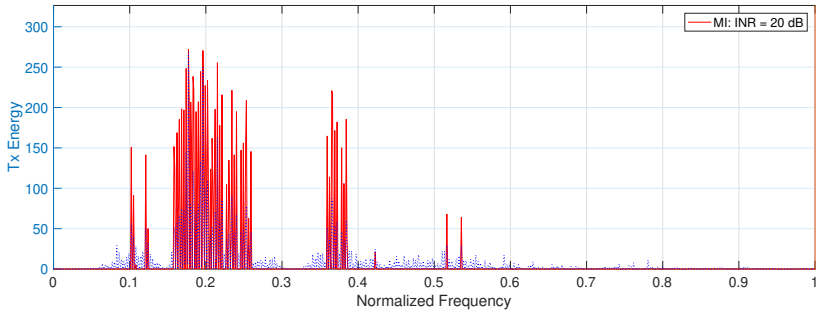

(b) E_x = 100 J and INR = 20 dB.

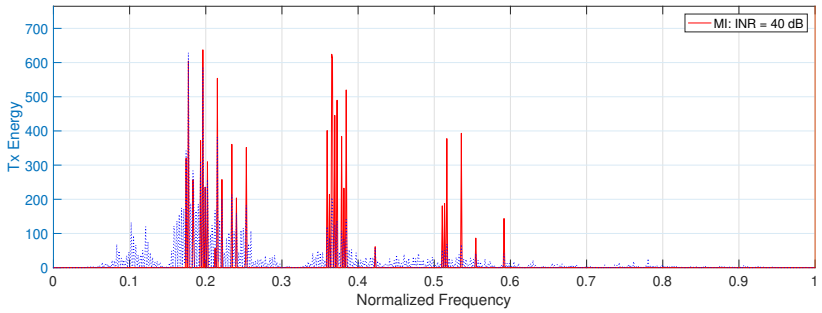

(c) E_x = 100 J and INR = 40 dB.

Figure 5.5. Mutual-Information Transmit Waveforms with Identical Energies in the Presence of Varying Ambient Noise INR

Table 5.1. Summary of P_D Gains for the Thermal-Noise Only Cases (P_D = 0.9.)

P_{FA}	Eigenwaveform	MI
10^{-2}	14.5 dB	12 dB
10^{-4}	11.5 dB	8 dB

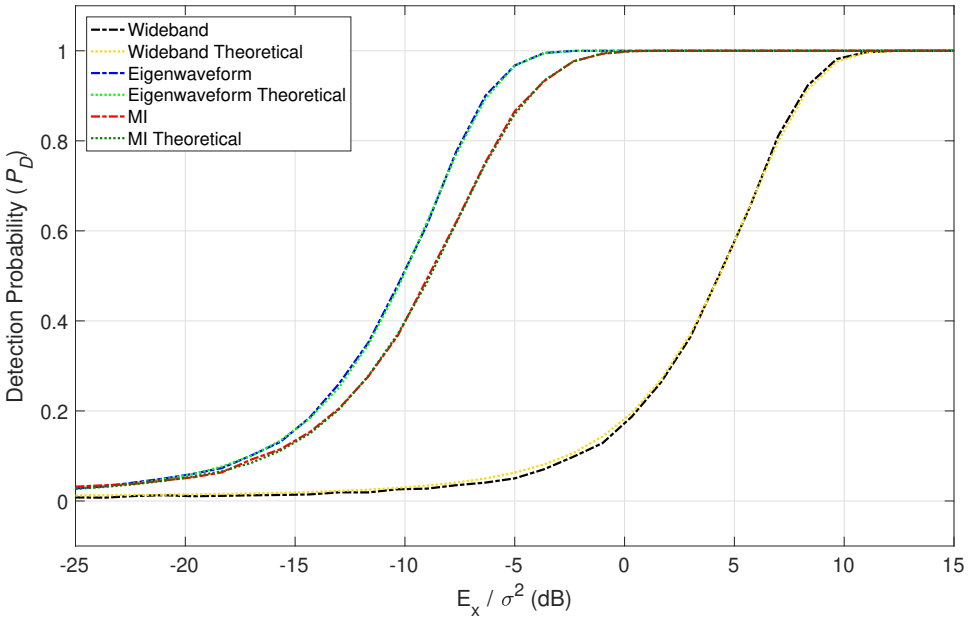

Figure 5.6. Detection Probability Curves, $P_{FA} = 10^{-2}$ (thermal noise only)

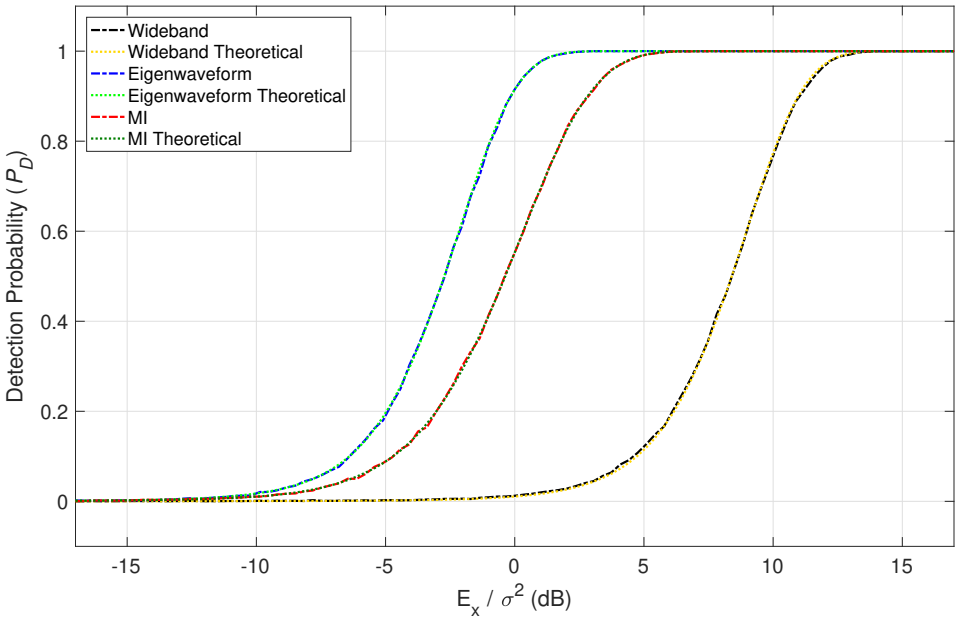

Figure 5.7. Detection Probability Curves, $P_{FA} = 10^{-4}$ (thermal noise only)

5.4.2 Thermal and Ambient Noise

The Monte Carlo simulations were then performed with the ambient noise included in the model. The eigenwaveform and MI waveform performances are compared to the performance of the wideband transmit signal to determine the P_D gain. The P_D results from the Monte Carlo simulations are represented by the dash-dot lines (blue, red, and black) in Figs. 5.8, 5.9, and 5.10 for a $P_{FA} = 10^{-2}$.

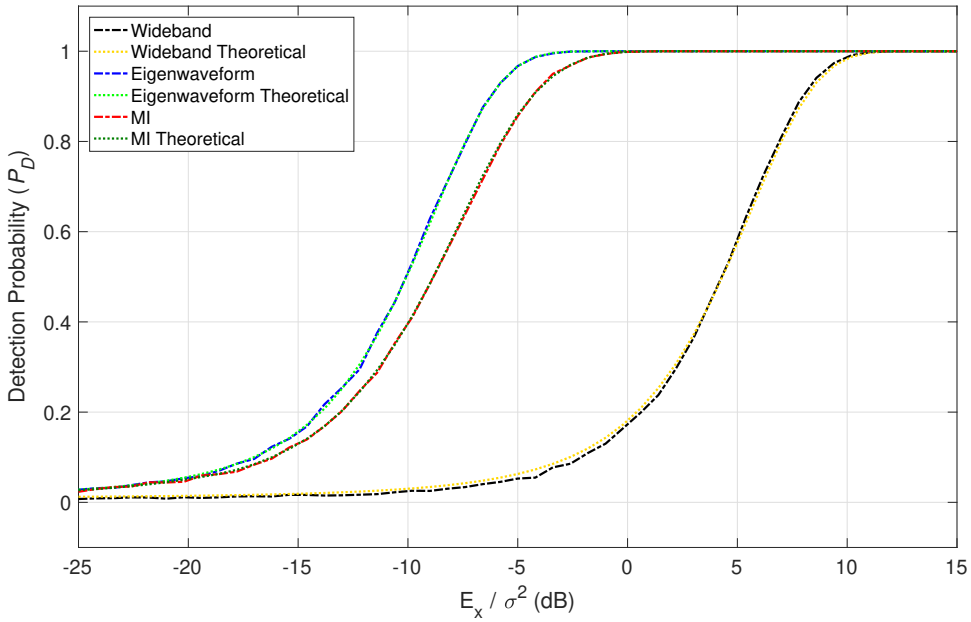

Figure 5.8. Detection Probability Curves for INR = 10 dB and $P_{FA} = 10^{-2}$ (thermal + ambient noise)

Similarly, for a $P_{FA} = 10^{-4}$, the P_D curves for all three INR cases are shown in Figs. 5.11, 5.12, and 5.13. Again, the theoretical closed-form expression for P_D (dotted line) validates the Monte Carlo simulations.

We see in Figs. 5.8 through 5.13 that the eigenwaveform and MI waveform for a fixed transmit energy yield higher detection probabilities. It is also apparent that the eigenwaveform consistently provides P_D gain over the wideband pulse across the three INR values. This is the result of the eigenwaveform's tendency to concentrate most of the transmit energy into one or a few dominant frequency bands that results in maximizing the SNR. Also, it is noted that the eigenwaveform's P_D gain increases when P_{FA} is increased to 10^{-2}. This

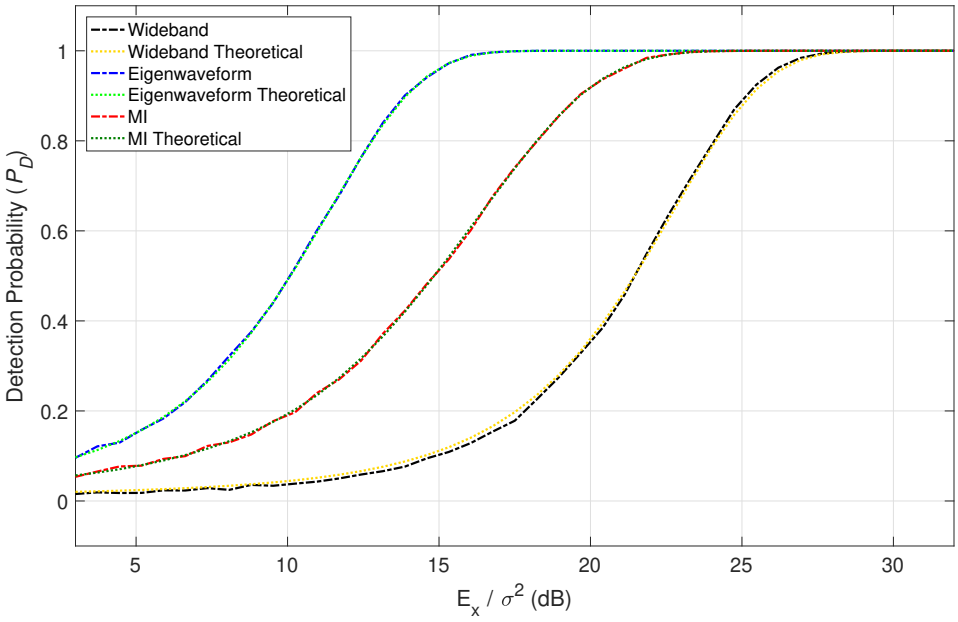

Figure 5.9. Detection Probability Curves for INR = 20 dB and $P_{FA} = 10^{-2}$ (thermal + ambient noise)

makes sense since an increased P_{FA} means a relaxation of the P_{FA} specification which in turn lowers the required threshold. A lower threshold allows for increased detection. It is also apparent that the the MI transmit waveform provides gain, but the gain decreases as the INR increases for both P_{FA} values. Focusing on a useful P_D of 0.9, the P_D gains are summarized in Table 5.2.

Table 5.2. Summary of P_D Gains for the Thermal Plus Ambient Noise Cases ($P_D = 0.9$.)

P_{FA}	INR	Eigenwaveform	MI
10^{-2}	10 dB	14.5 dB	12 dB
10^{-2}	20 dB	11.5 dB	5 dB
10^{-2}	40 dB	11.5 dB	2.5 dB
10^{-4}	10.5 dB	11 dB	7.5 dB
10^{-4}	20 dB	11 dB	4 dB
10^{-4}	40 dB	11 dB	1.5 dB

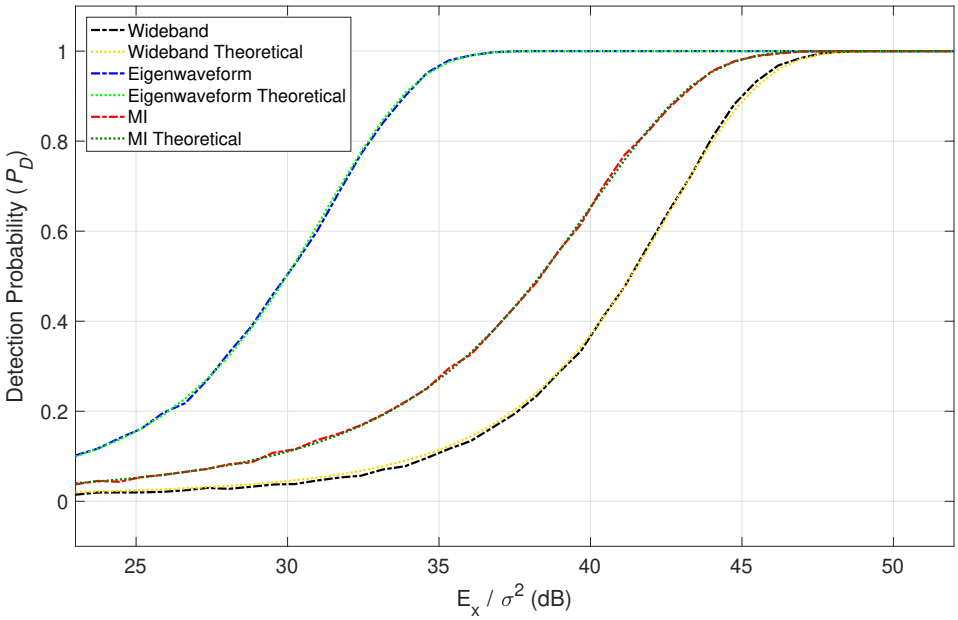

Figure 5.10. Detection Probability Curves for INR = 40 dB and $P_{FA} = 10^{-2}$ (thermal + ambient noise)

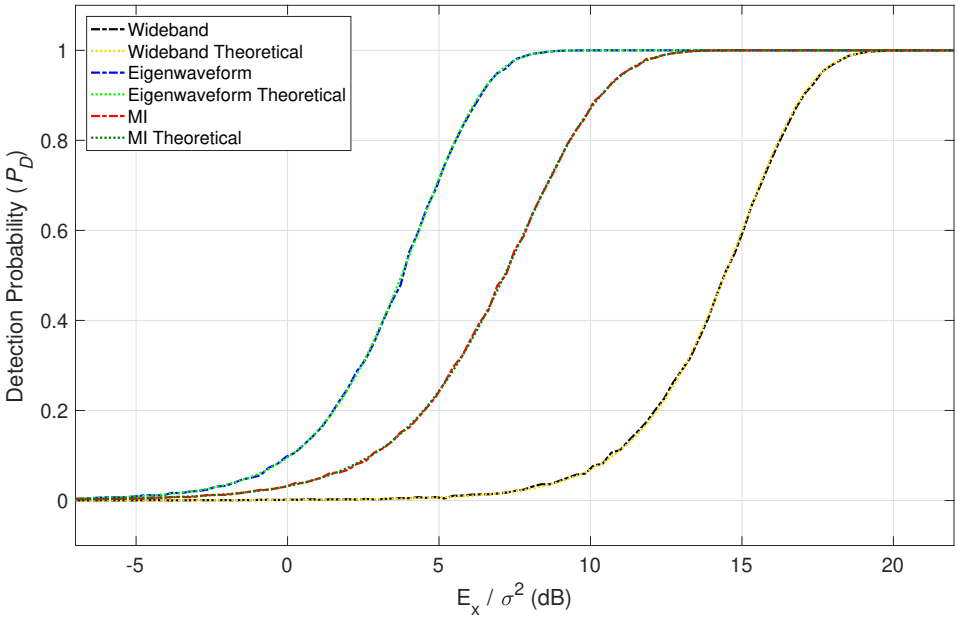

Figure 5.11. Detection Probability Curves for INR = 10 dB and $P_{FA} = 10^{-4}$ (thermal + ambient noise)

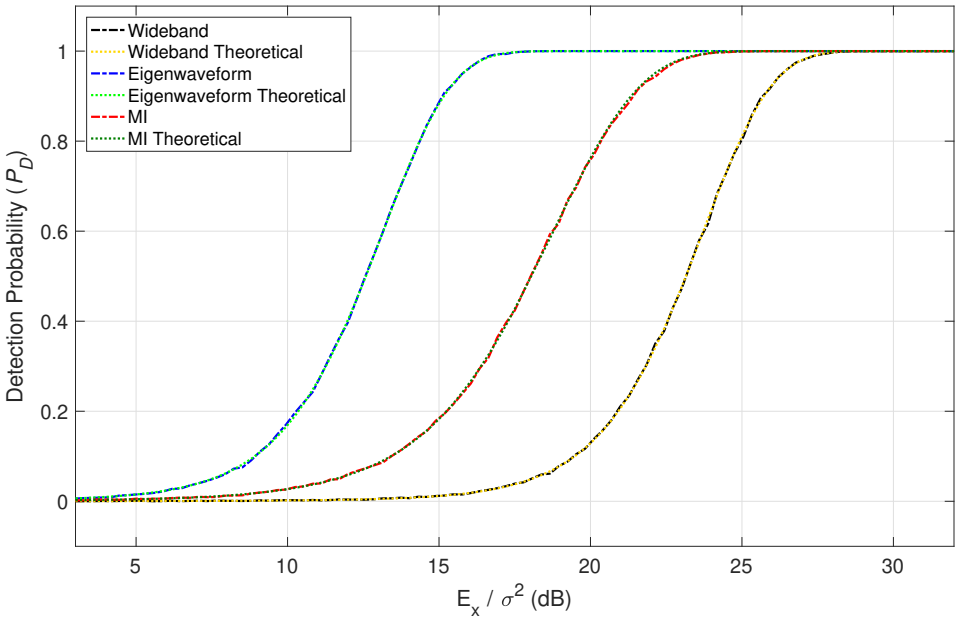

Figure 5.12. Detection Probability Curves for INR = 20 dB and $P_{FA} = 10^{-4}$ (thermal + ambient noise)

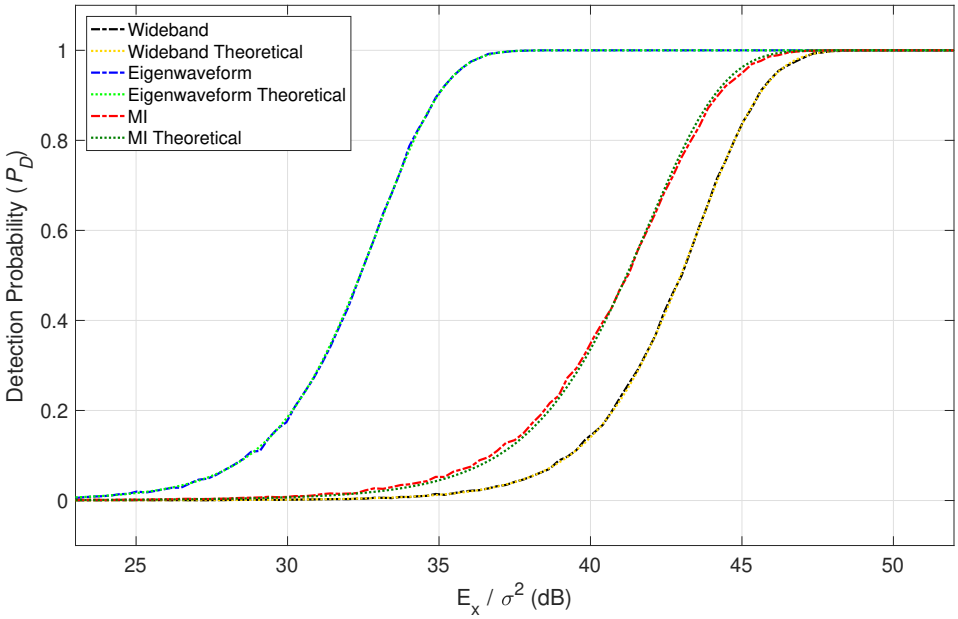

Figure 5.13. Detection Probability Curves for INR = 40 dB and $P_{FA} = 10^{-4}$ (thermal + ambient noise)

THIS PAGE INTENTIONALLY LEFT BLANK

CHAPTER 6:
Conclusions

6.1 Conclusion

In this thesis, we investigated the design of transmit waveforms matched to a particular target-channel response. An undersea channel was modeled with a full-wave solution to generate complex channel frequency responses. A realistic resonant spherical target, modeled after an early 20^{th}-century naval mine, was modeled to determine the scattering amplitude function. These responses were combined to yield a full-system frequency response. The two matched illumination transmit waveform design techniques were used, and their respective detection probability gains were analyzed. The behavior of the transmit eigenwaveforms and mutual-information waveforms were demonstrated for varying levels of ambient noise and transmit energy. The eigenwaveforms produced the largest gain in P_D. The MI waveform design technique was used to maximize the channel-target information and also yielded a gain in P_D. Monte Carlo simulations were used to verify the closed-form P_D expressions.

6.2 Future Work

The research in this thesis can be advanced by modeling more target shapes and investigating the corresponding detection probability gains. The investigation of objects with varying symmetries can be performed to analyze how aspect angle affects the gain.

Different undersea channel modeling methods can be explored that account for sound-speed profile gradients. Both the Navy Parabolic Equation model and the BellHop model can be used. Additionally, higher frequency ranges can be analyzed to investigate the usefulness of the optimized waveforms for high-frequency active sonar.

It should be noted that the frequency responses of the transmit and receive hydrophones were assumed to be flat. To account for realistic hydrophone characteristics, the frequency responses of the transmit and receive hydrophones could be incorporated in the system model.

The optimized waveforms used in this thesis can be further compared to waveforms like the CW, LFM, and other contemporary sonar transmit pulses.

Now that we have demonstrated the applicability of the optimized transmit waveforms for active sonar, further research can be performed to investigate the known advantages of the eigenwaveform and the MI transmit waveforms. The optimized transmit waveforms that were used in this thesis to increase detection probability can also be used for target classificaton. Applying the transmit waveforms for classification can yield cognitive active sonar that can discern between mine types, submarines, or other undersea objects.

List of References

[1] C. S. Clay, H. Medwin, *Acoustical Oceanography: Principles and Applications*, New York, NY, USA: John Wiley & Sons, 1977.

[2] L. J. Ziomek, *Fundamentals of Acoustic Field Theory and Space-Time Signal Processing*, Boca Raton, FL, USA: CRC Press, Inc. 1995.

[3] L. J. Ziomek, private communication, May 2018.

[4] R. R. Goodman, R. Stern, "Reflection and transmission of sound by elastic spherical shells," *The Journal of the Acoustical Society of America*, vol. 34, no. 3, pp. 338-344, 1962.

[5] T. K. Stanton, "Sound scattering by spherical and elongated shelled bodies," *The Journal of the Acoustical Society of America*, vol. 88, no. 3, pp. 1619-1633, 1990.

[6] R. A. Romero, J. Bae, N. A. Goodman, "Theory and application of SNR and mutual information matched illumination waveforms," *IEEE Trans. Aerospace and Electronic Systems*, vol. 47, no. 2, pp. 912-927, 2011.

[7] J. Pinto, D. A. Wiegand, "Yield and plastic flow in Composition B and TNT," U.S. Army Armament Research, Development and Engineering Center, Picatinny Arsenal, NJ, USA, January 1993.

[8] X. Lurton, *An Introduction to Underwater Acoustics: Principles and Applications*, Berlin, Springer-Verlag, 2010.

[9] G.M. Wenz, "Acoustic ambient noise in the ocean: Spectra and sources," *The Journal of the Acoustical Society of America*, vol. 34, no. 12, pp. 1936-1956, 1962.

[10] S. M. Kay, *Fundamentals of Statistical Signal Processing, Vol. II, Detection Theory*, Upper Saddle River, NJ, USA: Prentice-Hall PTR, 1998.

[11] Q. J. Tan, R. A. Romero, "Air vehicle target recognition with jammer nulling adaptive waveforms in cognitive radar using high-fidelity RCS responses," *IEEE International Conference on Radar*, Brisbane, Australia, August 2018.

[12] J. Nieh, R. A. Romero, “Comparison of ambiguity function of eigenwaveform to wideband and pulsed radar waveforms: a comprehensive tutorial,” *IET, The Journal of Engineering*, 2018.

Initial Distribution List

1. Defense Technical Information Center
   Ft. Belvoir, Virginia

2. Dudley Knox Library
   Naval Postgraduate School
   Monterey, California